PHOTONICS Research

Geometric metasurface for polarization synthesis and multidimensional multiplexing of terahertz converged vortices

Yang Zhu,[1] Binbin Lu,[1] Zhiyuan Fan,[1] Fuyong Yue,[1] Xiaofei Zang,[1,2,*] Alexei V. Balakin,[3] Alexander P. Shkurinov,[3] Yiming Zhu,[1,2,4] and Songlin Zhuang[1]

[1]Terahertz Technology Innovation Research Institute, Terahertz Spectrum and Imaging Technology Cooperative Innovation Center, Shanghai Key Laboratory of Modern Optical System, University of Shanghai for Science and Technology, Shanghai 200093, China
[2]Shanghai Institute of Intelligent Science and Technology, Tongji University, Shanghai 200092, China
[3]Department of Physics, Lomonosov Moscow State University, Moscow 119991, Russia
[4]e-mail: ymzhu@usst.edu.cn
*Corresponding author: xfzang@usst.edu.cn

Received 3 February 2022; revised 20 April 2022; accepted 20 April 2022; posted 21 April 2022 (Doc. ID 455459); published 31 May 2022

The investigation of converged twisted beams with a helical phase structure has a remarkable impact on both fundamental physics and practical applications. Geometric metasurfaces consisting of individually orientated metal/dielectric meta-atoms provide an ultracompact platform for generating converged vortices. However, it is still challenging to simultaneously focus left-handed and right-handed circularly polarized incident beams with pure geometric phase modulation, which hinders the independent operation on topological charges between these two helical components. Here we propose and experimentally demonstrate an approach to design terahertz geometric metasurfaces that can generate helicity-independent converged vortices with homogeneous polarization states by the superposition of two orthogonal helical vortices with identical topological charges. Furthermore, the multiplexing of polarization-rotatable multiple vortices in multiple dimensions, i.e., in both longitudinal and transverse directions, and a vortex with an extended focal depth is confirmed by embedding polarization modulation into the geometric metasurfaces. The demonstrated approach provides a new way to simultaneously manipulate orthogonal helical components and expand the design dimension, enabling new applications of geometric metasurface devices in polarization optics, twisted-beam related image and edge detection, high capacity optical communication, and quantum information processing, to name a few.

https://doi.org/10.1364/PRJ.455459

1. INTRODUCTION

Polarization and phase are two fundamental characteristics of electromagnetic (EM) waves, whose spatial distributions can be engineered to manipulate the properties of EM waves, leading to a variety of special beams, i.e., vortex beams [1] and vector vortex beams [2,3]. EM waves can possess spin angular momentum (SAM) and orbital angular momentum (OAM) states. SAM is associated with the circular polarization of EM waves, where the SAM of each photon is $\pm\hbar$. EM waves can also carry OAM with a helical phase defined as $\exp(il\theta)$, where l is the topological charge of the vortex beam. Since the OAM of EM waves has an infinite number of eigen modes, i.e., $l = \pm 1, \pm 2, \pm 3, \ldots$, and the different OAM modes are orthogonal, they possess unprecedented quantities of data for high-capacity data transmission in optical and quantum communication systems [4,5]. Currently, a variety of approaches, i.e., spiral phase plates [6], Q-plates [7], cylindrical mode converters [8], and spatial light modulators [9], have been developed to generate and manipulate vortex beams. However, all of these conventional methods for generating and manipulating multiple OAMs (e.g., superposition of OAM states) require many bulky components (functional devices) that need to be well aligned with each other. In addition, the aberrations induced by the mismatch or incompatibility between these individual components will inevitably degrade the quality of the generated vortex beams.

Geometric metasurfaces, which are composed of predesigned anisotropic meta-atoms with identical shapes but different in-plane orientations, provide a flexible platform to accurately tailor the amplitude, phase, and polarization of EM waves at subwavelength resolution. The manipulation of EM waves based on geometric metasurfaces depends on the spatially varying geometric phase response (Pancharatnam–Berry phase) rather than the phase (propagation phase) accumulation along optical paths. The main advantage of geometric metasurfaces is

the abrupt phase shifts that can be realized by anisotropic meta-atoms with thicknesses less than the wavelengths of EM waves, making geometric metasurfaces ideal candidates for device miniaturization and system integration. Benefiting from the ease of fabrication, ultrathin nature, and multifunctional integration characteristics, a plethora of applications, such as generalized Snell's law of refraction/reflection [10,11], metalenses [12–18], polarization manipulation [19–28], spin Hall effects [29–32], holograms [33–39], and nonlinear photonics [40–43], have been demonstrated. Moreover, by judiciously designing metasurfaces that introduce spatially varying geometric phase response, a variety of structured beams with various OAMs or topological charges have been demonstrated using circularly/linearly polarized incident beams, such as vortex beams [44–48], vector vortex beams [49], perfect vortex beams [50–54], and the multiplexing of multiple vortex beams [55–59]. However, previous studies of the multiplexing of vortices mainly focus on the transverse direction. The multiplexing of multiple vortex beams with polarization-controllable functionality in the longitudinal direction (or both transverse and longitudinal directions) offers further flexibilities to the manipulation of EM waves. Indeed, longitudinal multiplexing of multiple vortices can be realized by focusing spin-dependent vortices in the propagation direction, but the inherent conjugation in traditional geometric phase response between the two helical components hinders the simultaneous focusing and independent modulation of topological charges between left-handed circularly polarized (LCP) and right-handed circularly polarized (RCP) components.

In this paper, we propose an approach to design a geometric metasurface that can realize the polarization synthesis and multidimensional multiplexing of terahertz converged vortices, based only on the geometric phase response. The polarization-independent converged vortices are first demonstrated by the superposition of two converged vortices with orthogonal circularly polarized (CP) states and identical topological charges. By further integrating the multiple focusing phases and polarization-rotatable functionality into a single geometric metasurface, the multiplexing of polarization-rotatable multiple vortices in the longitudinal direction or multiple dimensions (both transverse and longitudinal directions) has been realized. Furthermore, a converged vortex beam with an extended focal depth is realized through a partial overlap of two orthogonal linearly polarized (LP) vortices. This robust approach for superposition and multiplexing of THz converged vortices enables a far-reaching impact on designing flat devices with multiple functionalities and applications in polarization-dependent sensing or imaging, detection, and quantum information.

2. PRINCIPLE AND DESIGN

The operating principle for superposition and multiplexing of THz converged vortices is schematically shown in Fig. 1. As depicted in Fig. 1(a), a metasurface is designed to focus the incident THz waves with arbitrary polarization states into a converged vortex with identical topological charges. The incident THz waves can be divided into two orthogonal circular components (LCP and RCP). To simultaneously focus the LCP and RCP components into a converged vortex with the same topological charge, the required phase profile for the geometric metasurface is governed by [55,60]

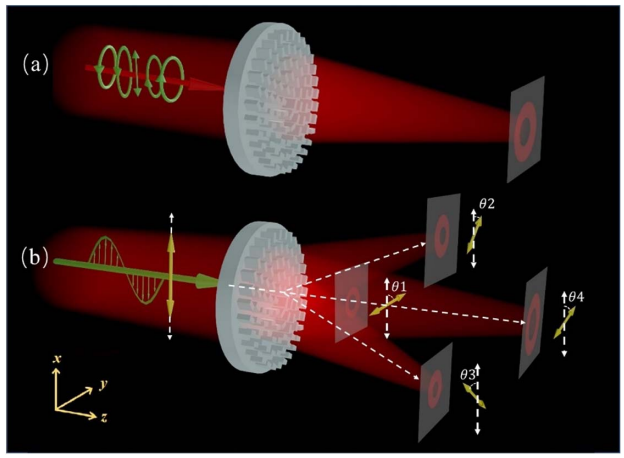

Fig. 1. Schematic of the metasurfaces for polarization-independent vortex and the multiplexing of polarization-rotatable multiple vortices in multiple spatial dimensions. (a) Polarization-independent vortex with identical topological charges generated by a geometric metasurface under illumination of THz waves with arbitrary polarization states. (b) Multiplexing of polarization-rotatable multiple vortices in both transverse and longitudinal directions under illumination of linearly polarized THz waves.

$$\Phi_1 = \arg[\exp(i\varphi_{\mathrm{LCP}}) + \exp(i\varphi_{\mathrm{RCP}})], \tag{1}$$

where $\varphi_{\mathrm{LCP}} = \frac{2\pi}{\lambda}(\sqrt{x^2 + y^2 + f_L^2} - f_L) + l_L\varphi$ and $\varphi_{\mathrm{RCP}} = -\frac{2\pi}{\lambda}(\sqrt{x^2 + y^2 + f_R^2} - f_R) - l_R\varphi$. "Arg" returns the phase angles of the total field of "$\exp(i\varphi_{\mathrm{LCP}}) + \exp(i\varphi_{\mathrm{RCP}})$". f_L and f_R are the focal lengths of the converged RCP and LCP vortices, respectively, and l_L and l_R are topological charges. λ is the working wavelength. When $f_l = f_R$ and $l_L = l_R = l$, a converged vortex with a topological charge of l can be observed after the metasurface under illumination of a THz wave with an arbitrary polarization state. It should be noticed that the phase profile in Eq. (1) contains a convex lens and a concave lens relative to both incident LCP and RCP components, and thus the spin-independent converged vortex can be generated by the designed metasurface. For the incidence of LCP/RCP THz waves, it is modulated by both φ_{LCP} (for focusing the incident LCP/RCP THz waves into an RCP/LCP converged vortex) and φ_{RCP} (for defocusing it into background). Only half of the transmitted waves will be converted to the RCP/LCP converged vortex. Therefore, the maximal focusing efficiency of the designed metasurfaces cannot exceed 50% in theory.

Since the incident LCP and RCP components with the same amplitude can be combined (by the metasurface) into an LP converged vortex, our approach can be extended to generate a polarization-rotatable converged vortex by embedding polarization modulation into the geometric metasurfaces. The phase requirement can be expressed as

$$\Phi_2 = \arg\left\{\exp\left\{i\left[\frac{2\pi}{\lambda}\left(\sqrt{x^2+y^2+f_L^2}-f_L\right)+l_L\varphi\right]+\phi\right\} + \exp\left\{-i\left[\frac{2\pi}{\lambda}\left(\sqrt{x^2+y^2+f_R^2}-f_R\right)+l_R\varphi\right]-\phi\right\}\right\}. \quad (2)$$

According to Eq. (2), the converged vortex after the metasurface will be generated with the corresponding polarization state (LP state) rotated with an angle ϕ in comparison with the incident THz waves. Furthermore, we can integrate a series of converged vortices with different orientations of polarization into a single metasurface to realize the multiplexing of polarization-rotatable multiple vortices on multiple spatial dimensions [see Fig. 1(b)]. The phase profile of the geometric metasurface can be written as

$$\Phi_3 = \arg\left\{\sum_{i=1}^{N}[\exp(i\varphi_{i\text{-LCP}}) + \exp(i\varphi_{i\text{-RCP}})]\right\}, \quad (3)$$

where $\varphi_{i\text{-LCP}} = \left\{\frac{2\pi}{\lambda}\left[\sqrt{(x-x_{i\text{-}L})^2+(y-y_{i\text{-}L})^2+f_{i\text{-}L}^2}-f_{i\text{-}L}\right]+l_{i\text{-}L}\varphi\right\}+\phi_i$ ($\varphi_{i\text{-LCP}}$ is the phase profile for converting the LCP incident beam into the ith RCP converged vortex), and $\varphi_{i\text{-RCP}} = -\left\{\frac{2\pi}{\lambda}\left[\sqrt{(x-x_{i\text{-}R})^2+(y-y_{i\text{-}R})^2+f_{i\text{-}R}^2}-f_{i\text{-}R}\right]+l_{i\text{-}R}\varphi\right\}+\phi_i$ ($\varphi_{i\text{-RCP}}$ is the required phase profile for converting the RCP incident beam into the ith LCP converged vortex). $i = 1, 2, 3, \ldots$, and $f_{i\text{-}L} = f_{i\text{-}R}$ (defined as the focal length of the ith LCP and RCP converged vortex). A detailed discussion of the metasurfaces for generating multiple converged vortices with polarization-rotatable functionality is given in Appendix A.

We design a series of silicon-based geometric metasurfaces to demonstrate the aforementioned functionalities. As shown in Fig. 2(a), the silicon-based dielectric metasurface consists of anisotropic meta-atoms with identical shapes but different orientations. Each meta-atom should be optimized as a quasi-half-wave plate that can switch the incident LCP (RCP) THz waves into RCP (LCP) beams with an abrupt phase change (Pancharatnam–Berry phase). The optimized structure parameters of the meta-atom are $L = 80$ μm, $W = 42$ μm, $h_1 = 400$ μm, and $h_2 = 600$ μm. When the long axis of the meta-atom is placed along the x axis, the transmittance between transverse magnetic (TM) and transverse electric (TE) waves is the same at $f = 0.8$ THz (working frequency), and the phase difference between the transmitted TE and TM waves is about π, which demonstrates that our designed meta-atom works as a quasi-half-wave plate [see the dark and green lines in Fig. 2(b)]. Under illumination of an LCP THz beam, the transmittance of RCP THz waves at 0.8 THz is nearly 90%, which can be defined as conversion efficiency (the ratio between the power of transmitted cross-polarized THz waves and incident power). The oscillations in transmission [see Fig. 2(b)] can be qualitatively explained as Fabry–Perot resonance, as in Ref. [44]. Figures 2(c)–2(f) show fabricated samples for generating the spin-independent vortex [Fig. 2(c)], the multiplexing of polarization-rotatable vortices in the longitudinal direction [Fig. 2(d)], multiple spatial dimensions [Fig. 2(e)], and the vortex with an extended focal depth [Fig. 2(f)].

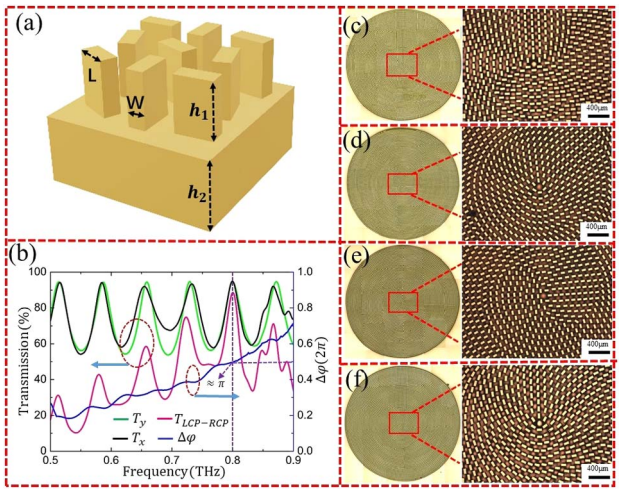

Fig. 2. Design and fabrication of the geometric metasurfaces. (a) Designed geometric metasurface consisting of meta-atoms with identical shapes but different in-plane orientations. (b) Transmission spectra (green and black curves) and phase difference (blue curve) of a meta-atom with the long-axis along the x axis for the incidence of transverse electric and transverse magnetic modes. Polarization conversion efficiency for the incidence of LCP waves is depicted as the pink curve. (c)–(f) Fabricated samples to realize the spin-independent vortex (c), multiplexing of polarization-rotatable vortices in the longitudinal direction (d) and multiple spatial dimensions (e), and the vortex with extended focal depth (f).

3. RESULTS

As a guiding study, the generation of a polarization-independent THz vortex based on the designed metasurface [see Fig. 2(c)] is initially demonstrated. As depicted in Eq. (1), the phase profile induced by each meta-atom contains a spiral phase and focusing functionality for both LCP and RCP components. The corresponding focal length is theoretically designed as $f = 8$ mm, and the topological charge of the polarization-independent THz vortex is $l_L = l_R = 1$. Figure 3 shows numerical simulations and experimental results of our designed metasurface for generating the polarization-independent THz vortex. Under illumination of LCP THz waves, we calculate the corresponding electric-field intensity and phase distributions, as shown in Figs. 3(a_1) and 3(b_1). A converged vortex (at $f = 0.8$ THz) can be observed after the metasurface, and the focal length is about $z = 7.5$ mm. There is a slight discrepancy in focal length between the calculated result and theoretical case that can be attributed to the finite meta-atoms in numerical simulations (100 meta-atoms in the radial direction). The phase distribution illustrated in Fig. 3(b_1) shows a 2π phase change around point (0, 0, 7.5 mm), which demonstrates that the converged vortex possesses a topological charge of $l = 1$. Figures 3(c_1) and 3(d_1) show the measured results of the fabricated sample [see Fig. 2(c)]. A converged vortex is generated after the sample with the focal length of $z = 7.5$ mm [see Fig. 3(c_1)]. The measured

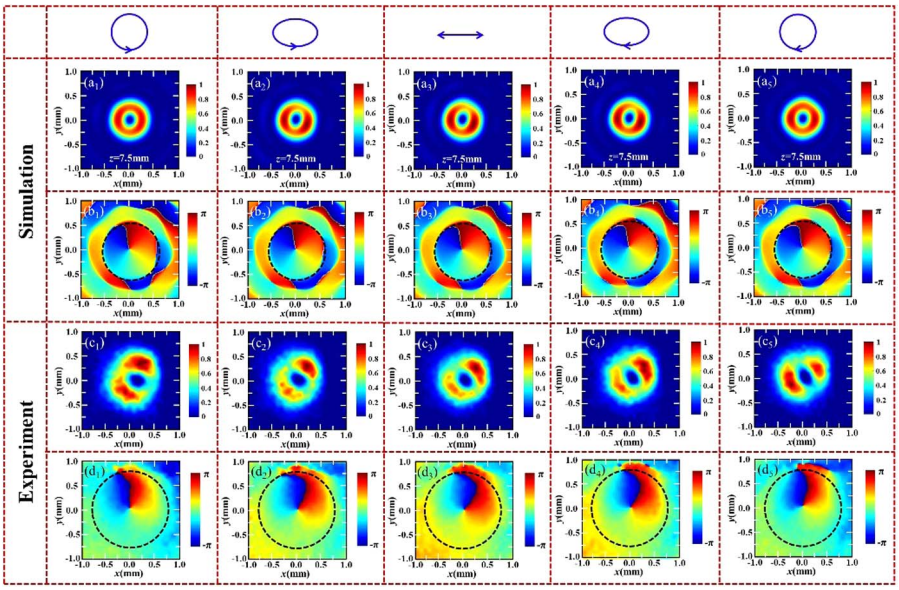

Fig. 3. Electric-field intensity and phase distributions of the spin-independent vortices. (a_1)–(a_5), (c_1)–(c_5) Simulated and measured electric-field intensity distributions after the designed geometric metasurface under illumination of LCP, LECP, LP, RECP, and RCP THz waves. (b_1)–(b_5), (d_1)–(d_5) Simulated and measured phase distributions of the corresponding vortices.

phase distribution in the focal plane ($z = 7.5$ mm) shows that the phase change around point (0, 0, 7.5 mm) is also 2π. Therefore, a converged vortex with a topological charge of one is experimentally demonstrated. In comparison with Figs. 3(a_1) and 3(b_1) and Figs. 3(c_1) and 3(d_1), the numerical simulations agree well with the measured results, except for a slight mismatch in field and phase distributions, which can be ascribed to sample imperfection. Figures 3(a_2)–3(d_5) show the numerical calculations and measured results of the electric-field intensity and phase distributions under the illumination of THz waves with polarization switched from left-handed elliptically polarized (LECP) state to RCP state. One converged vortex with a focal length of $z = 7.5$ mm and the corresponding topological charge of $l = 1$ is observed after the geometric metasurface for the incidence of THz waves with an arbitrary polarization state. The designed geometric metasurface can focus both LCP and RCP components into a converged vortex (located at the same position) with the same topological charge, which demonstrates that the proposed approach can simultaneously focus and independently modulate the topological charges of the two helical components. The electric-field intensity distributions of the polarization-independent converged vortex in the x–z plane are given in Appendix B.

The polarization-independent characteristic demonstrated above can indeed be realized by designing a metasurface with isotropic meta-atoms, i.e., symmetric cylindrical or square-shaped meta-atoms with different sizes, but that method loses a degree-of-freedom in the design space, due to the limited tailoring functionality (on the wavefront of EM waves) of isotropic meta-atoms. The proposed method based on geometric metasurfaces consisting of anisotropic meta-atoms cannot only independently focus two orthogonal helical components into a converged vortex, but also enable the capability to rotate the orientation of polarization, resulting in polarization-rotatable converged vortex/vortices. As depicted in Eq. (2), an angle (ϕ) of polarization rotation is introduced into the phase profile to rotate the polarization of the converged vortex. When $\phi = 90°$ and under illumination of x-polarized THz waves, a y-polarized converged vortex can be observed behind the designed geometric metasurface. The electric-field intensity and phase distributions of such a polarization-rotatable converged vortex are shown in Appendix C.1. By integrating the multiple focusing phases and spiral phases, and the polarization-rotation modulations into a geometric metasurface, the multiplexing of multiple converged vortices with polarization-rotatable functionality can be realized [see Eq. (3)]. Figure 4 shows the demonstration of two longitudinally multiplexed converged vortices with two orthogonal LP states. The designed phase parameters are $x_{1\text{-}L} = x_{1\text{-}R} = y_{1\text{-}L} = y_{1\text{-}R} = 0$, $x_{2\text{-}L} = x_{2\text{-}R} = y_{2\text{-}L} = y_{2\text{-}R} = 0$, $f_{1\text{-}L} = f_{1\text{-}R} = 4.5$ mm, $f_{2\text{-}L} = f_{2\text{-}R} = 8.5$ mm, $\phi_1 = 0°$, and $\phi_2 = 90°$. For the incidence of x-polarized THz waves, an x-polarized converged THz vortex is observed with a focal plane at $z = 4.3$ mm, as shown in Fig. 4(a_1). In addition, another converged vortex is coaxially located at the focal plane of $z = 7.9$ mm, but the corresponding polarization state of such a converged vortex is rotated counterclockwise with an angle of 90° in comparison to that of the incident THz waves, resulting in a y-polarized (converged) vortex [see Fig. 4(a_2)]. The simulated phase distributions in Figs. 4(a_3) and 4(a_4) show that both multiplexed converged vortices in the longitudinal direction have the same topological charge of one. The electric-field intensity distributions in the x–z plane of these two converged vortices are illustrated in Figs. 4(a_5) and 4(a_6). The main intensity distribution of the left converged vortex ranges from $z = 3.8$ mm to $z = 5$ mm, while it is located between $z = 7$ mm and $z = 9$ mm for the right one, which demonstrates two separated vortices in the longitudinal direction. Figures 4(b_1)–4(b_6) show the measured

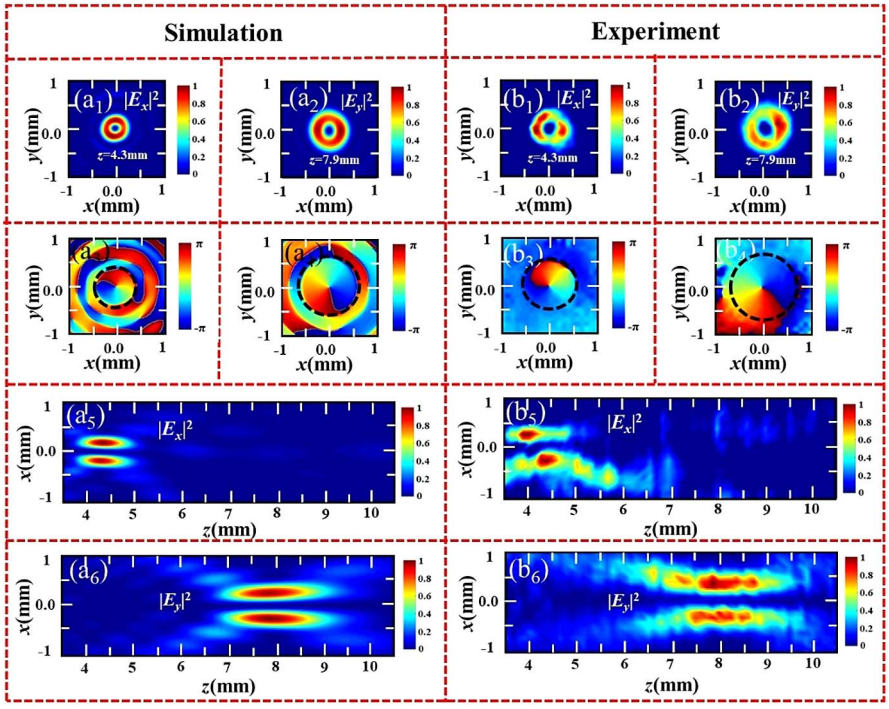

Fig. 4. Electric-field intensity and phase distributions of the multiplexing of two vortices with two orthogonal LP states in the longitudinal direction. (a_1)–(b_2) Simulated and measured electric-field intensity distributions at $z = 4.3$ mm and $z = 7.9$ mm, respectively. (a_3)–(b_4) Corresponding phase distributions for (a_1)–(b_2). (a_5)–(b_6) Simulated and measured electric-field intensity distributions in the x–z plane.

electric-field intensity and phase distributions. Under the illumination of an x-polarized THz beam, there is one x-polarized converged vortex and one y-polarized (converged) vortex after the fabricated sample. The focal lengths of both converged vortices corresponding to two orthogonal polarization states are $z = 4.3$ mm and $z = 7.9$ mm, respectively [see Figs. 4(b_1) and 4(b_2)]. The topological charge of each vortex is one [see Figs. 4(b_3) and 4(b_4)]. The main electric-field intensity distribution of the vortex on the left (or right) side is located from 3.5 mm (6.0 mm) to 5.8 mm (9.5 mm), which also demonstrates that two separated vortices in the longitudinal direction are observed in experiment [see Figs. 4(b_5) and 4(b_6)]. The multiplexing of an x-polarized vortex and a y-polarized vortex in the transverse direction is supplied in Appendix C.2. In addition, the multiplexing of two vortices with two orthogonal helical states (LCP and RCP) in the longitudinal direction (or transverse direction) is given in Appendix C.3 and Appendix C.4.

To further demonstrate the unique and robust characteristic of our proposed approach, the multiplexing of vortex superposition in both transverse and longitudinal directions is calculated and experimentally investigated in Fig. 5. The structure parameters in this case are designed as $x_{1\text{-}L} = x_{1\text{-}R} = y_{1\text{-}L} = y_{1\text{-}R} = 0$, $x_{2\text{-}L} = x_{2\text{-}R} = y_{2\text{-}L} = y_{2\text{-}R} = 0$, $f_{1\text{-}L} = f_{1\text{-}R} = 4.5$ mm, $f_{2\text{-}L} = f_{2\text{-}R} = 8.5$ mm, $\phi_1 = \phi_2 = 90°$, $x_{3\text{-}L} = x_{3\text{-}R} = 1.5$ mm, $x_{4\text{-}L} = x_{4\text{-}R} = -1.5$ mm $y_{3\text{-}L} = y_{3\text{-}R} = y_{4\text{-}L} = y_{4\text{-}R} = 0$, $f_{3\text{-}L} = f_{4\text{-}R} = 6.5$ mm, and $\phi_3 = \phi_4 = 0°$. Under illumination of x-polarized THz waves, two x-polarized converged vortices are symmetrically distributed along the x axis, as shown in Figs. 5(a_1) and 5(a_2). One vortex is located at (1.5 mm, 0, 6.3 mm), and the other vortex is placed at (−1.5 mm, 0, 6.3 mm). The topological charge of each vortex is one [see Figs. 5(d_1) and 5(d_2)]. Since these two converged vortices possess the same focal plane ($z = 6.3$ mm), the multiplexing of vortices in the transverse direction is realized. In contrast, when the y-polarized electric-field intensity is calculated and measured, two coaxially distributed converged vortices can be observed in the longitudinal direction [see Figs. 5(b_1), 5(b_2), 5(c_1), and 5(c_2)]. One vortex is focused at the focal plane of $z = 4.3$ mm, while the other one is coaxially located at the focal plane of $z = 7.9$ mm. The polarizations of these two longitudinal multiplexed converged vortices are orthogonal to those of the incident THz waves. Both x-polarized and y-polarized electric-field intensities in the x–z plane [see Figs. 5(g_1), 5(g_2), 5(h_1), and 5(h_2)] show that two separated transversely distributed and longitudinally distributed converged vortices are generated by combining the modulations of focusing phases, spiral phases, and polarization-rotatable modulations. The multiplexing of multiple vortices with LP and CP states is also demonstrated and given in Appendix D. In addition, the multiplexing of multiple (converged) vortices with CP or LP states and different topological charges is supplied in Appendix E.

4. DISCUSSION AND CONCLUSION

The converged vortex/vortices realized by combining the functionalities of a lens and a vortex plate into geometric metasurfaces can be potentially used in imaging, in particular, for edge detection and edge imaging, which will boost the efficiency of

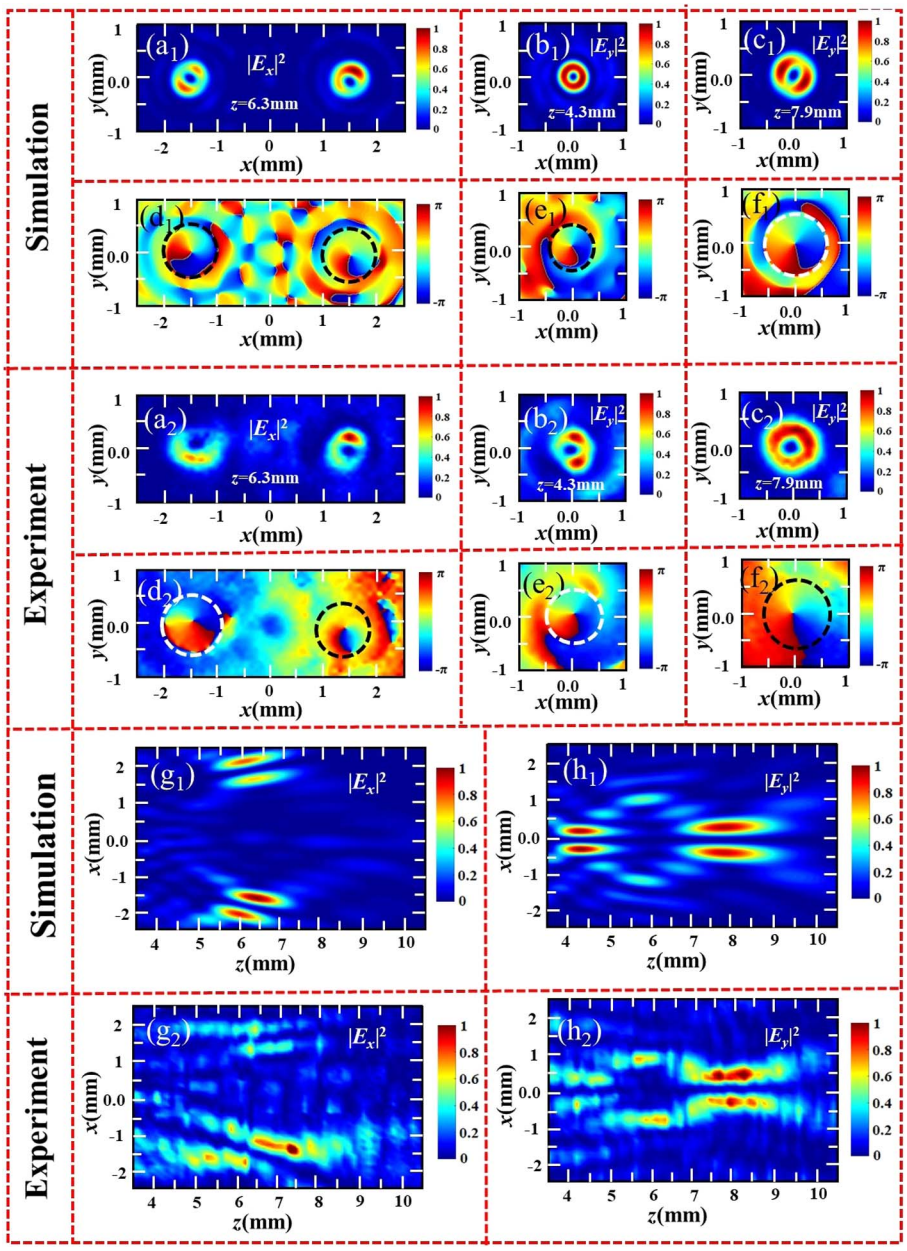

Fig. 5. Electric-field intensity and phase distributions of the multiplexing of four vortices with different LP states in longitudinal and transverse directions. (a_1)–(f_2) Simulated and measured electric-field intensity and phase distributions at $z = 4.3$ mm, $z = 6.3$ mm, and $z = 7.9$ mm, respectively. (g_1)–(h_2) Simulated and measured electric-field intensity distributions in the x–z plane.

computer vision applications. However, traditional focal points or converged vortex/vortices are limited to the chromatic aberration due to the finite focal depth. A converged vortex with an extended focal depth can further tolerate focal shifts, and thus, it can be applied in high-tolerance edge imaging. As a proof of concept, a converged vortex with an extended focal depth is demonstrated, as shown in Fig. 6. The designed geometric metasurface can focus LP THz waves into two coaxially distributed converged vortices, and hence, one can generate two converged vortices with partial overlapping to each other, leading to the converged vortex with an extended focal length. The structure parameters are $x_{1\text{-}L} = x_{1\text{-}R} = y_{1\text{-}L} = y_{1\text{-}R} = 0$, $x_{2\text{-}L} = x_{2\text{-}R} = y_{2\text{-}L} = y_{2\text{-}R} = 0$, $f_{1\text{-}L} = f_{1\text{-}R} = 7.0$ mm, $f_{2\text{-}L} = f_{2\text{-}R} = 8.5$ mm, $\phi_1 = 0°$, and $\phi_2 = 90°$. As depicted in Fig. 6(a_1), an x-polarized vortex with the main electric-field intensity distribution ($|E_x|^2$) ranging from 5.8 mm to 7.6 mm is observed. In addition, a y-polarized converged vortex is also generated after the designed geometric metasurface. The main electric-field intensity distribution ($|E_y|^2$) is located between $z = 7$ mm and $z = 9.1$ mm [see Fig. 6(b_1)]. In comparison with Figs. 6(a_1) and 6(b_1), both the x-polarized and y-polarized converged vortices are partially overlapped with each other. As a result, a converged vortex with an extended focal length can be realized with the main electric-field intensity distribution

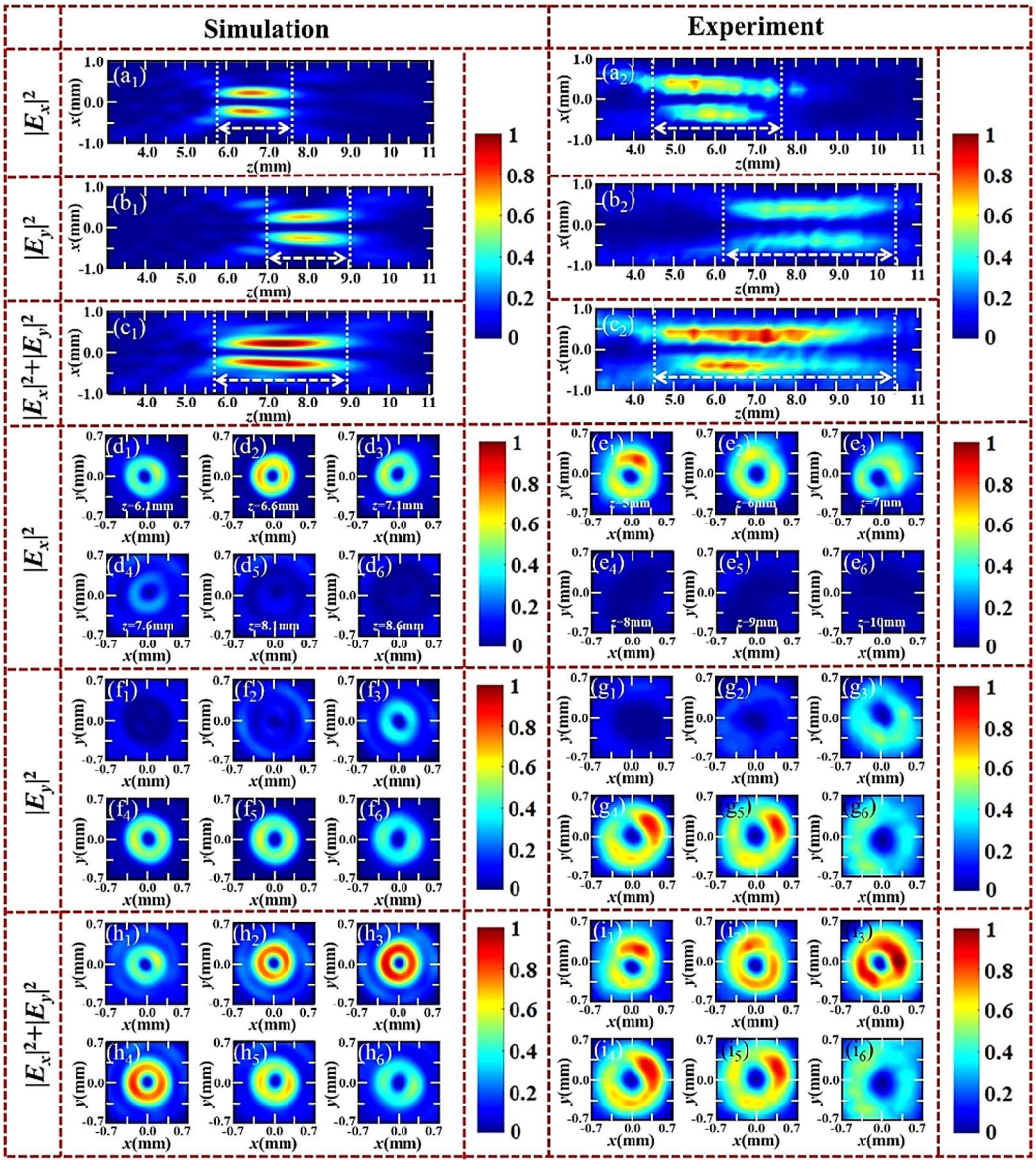

Fig. 6. Electric-field intensity distributions of a vortex with extended focal length. (a_1)–(c_2) Simulated and measured electric-field intensity distributions for $|E_x|^2$, $|E_y|^2$, and $|E_x|^2 + |E_y|^2$ in the x–z plane. (d_1)–(e_6), (f_1)–(g_6), and (h_1)–(i_6) Simulated and measured electric-field intensity distributions for $|E_x|^2$, $|E_y|^2$, and $|E_x|^2 + |E_y|^2$ in different x–y planes.

($|E_x|^{2+}|E_y|^2$) ranging from 5.8 mm to 9.0 mm [see the total electric-field intensity distribution in Fig. 6(c_1)]. The electric-field intensity distributions in the x–y plane for $|E_x|^2$, $|E_y|^2$, and $|E_x|^2 + |E_y|^2$ are shown in Figs. 6(d_1)–6(h_3). Three x-polarized converged vortices and four y-polarized converged vortices can be observed in different x–y planes, while seven converged vortices are revealed in the total electric-field intensity distributions. The measured results are shown in Figs. 6(a_2)–6(i_6). The x-polarized converged vortex is mainly distributed from 4.5 mm to 7.6 mm [see Fig. 6(a_2)], while the y-polarized converged vortex is mainly located between 6.2 mm and 10.4 mm [see Fig. 6(b_2)]. The total electric-field intensity distribution in experiment ranges from 4.5 mm to 10.6 mm, demonstrating a converged vortex with an extended focal length [see Fig. 6(c_2)]. The measured electric-field intensity distributions in the x–y plane for $|E_x|^2$, $|E_y|^2$, and $|E_x|^2 + |E_y|^2$ are shown in Figs. 6(e_1)–6(i_6), and they are also confirmed as a converged vortex with an extended focal length. The calculated and measured phase distributions in the x–y plane are given in Appendix F.

In fact, a vortex enables the functionality in manipulating micro-particles. Our proposed geometric metasurfaces for generating converged vortices with well-defined focal planes provide a compact platform and an essential ingredient for preferably trapping and rotating micro-particles, especially for polarization-dependent micro-particles. Since a vortex can be applied to edge imaging/detection [61] based on a Fourier transform setup incorporating metasurfaces (that can generate

a vortex), our proposed geometric metasurfaces for generating multiple converged vortices can be extended to realize multifocal edge imaging/detection [62]. Furthermore, the proposed geometric metasurface that can generate a vortex with an extended focal length can further successively mitigate aberrations, leading to applications in high-tolerance edge imaging/detection [63] in the longitudinal direction.

In summary, we have proposed and experimentally demonstrated an approach to the independent manipulation of two orthogonal helical components of THz waves. By integrating the focusing functionality and spiral phases into a geometric metasurface, the polarization-independent vortex was realized by the superposition of two orthogonal helical vortices with identical topological charges. Although the combination of geometric phase and propagation phase can be applied to independently manipulate these two orthogonal helical components, it suffers from the disadvantage of scanning a large number of structural parameters of meta-atoms to achieve locally customized objectives of spatial phase sampling. In addition, the proposed geometric metasurface enables the polarization-rotatable functionality by unitarily rotating each meta-atom. The multiplexing of multiple polarization-controllable vortices in the longitudinal/transverse direction or both longitudinal and transverse directions has been realized by introducing multiple focusing and spiral phases and polarization-rotatable functionality into the geometric metasurface. Finally, a vortex with an extended focal length was further demonstrated. This unique and robust approach provides a platform for integrating multiple functionalities into a single metasurface, leading to the straightforward design and miniaturization of multifunctional optical devices and systems.

APPENDIX A: PRINCIPLES OF POLARIZATION-ROTATABLE FUNCTIONALITY AND MULTIPLEXING OF THz CONVERGED VORTICES

As shown in Fig. 7(a), an anisotropic meta-atom can be used as a half-wave plate with the functionality expressed by the Jones matrix

$$P = \begin{bmatrix} p_x & 0 \\ 0 & p_y \end{bmatrix}, \qquad 0 \le p_{x,y} \le 1, \tag{A1}$$

where p_x and p_y are transmittances of the polarizer along the x and y axes, respectively. If the meta-atom is rotated counterclockwise with an angle of $\frac{\phi}{2}$ [see Fig. 7(b)], the Jones matrix can be written as

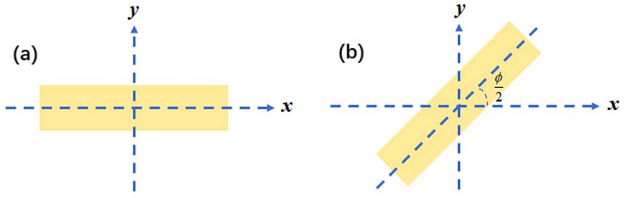

Fig. 7. Schematics of anisotropic meta-atoms without (a) and with (b) a rotation angle.

$$\begin{aligned} J' &= J\left(-\frac{\phi}{2}\right) P J\left(\frac{\phi}{2}\right) \\ &= \begin{bmatrix} \cos\frac{\phi}{2} & -\sin\frac{\phi}{2} \\ \sin\frac{\phi}{2} & \cos\frac{\phi}{2} \end{bmatrix} \begin{bmatrix} p_x & 0 \\ 0 & p_y \end{bmatrix} \begin{bmatrix} \cos\frac{\phi}{2} & \sin\frac{\phi}{2} \\ -\sin\frac{\phi}{2} & \cos\frac{\phi}{2} \end{bmatrix}. \end{aligned} \tag{A2}$$

The electric field of a CP beam passing through the polarizer can be expressed as

$$\begin{aligned} E_{\mathrm{RCP/LCP}} &= J' \frac{1}{\sqrt{2}} \begin{bmatrix} 1 \\ \pm i \end{bmatrix} \\ &= \frac{p_x + p_y}{2} \frac{1}{\sqrt{2}} \begin{bmatrix} 1 \\ \pm i \end{bmatrix} + \frac{p_x - p_y}{2} e^{\pm i\phi} \frac{1}{\sqrt{2}} \begin{bmatrix} 1 \\ \mp i \end{bmatrix}. \end{aligned} \tag{A3}$$

As depicted in Eq. (A3), one part of the incident CP beam is converted into the cross-polarized component with an additional phase of $\pm\phi$ ($\pm$ is dependent on the chirality of the incident CP beam), and the other part is still the co-polarized component. When the phase difference $\Delta\varphi = \varphi_x - \varphi_y$ between the fast and slow axes of the polarizer is π, it can be considered as a half-wave plate, and thus, $p_x = e^{i\frac{\pi}{2}} = i$, $p_y = e^{-i\frac{\pi}{2}} = -i$, $p_x + p_y = 0$, and $p_x - p_y = 2i$. Under the illumination of an LP beam, the orientation of polarization (of the converted beam) will be rotated clockwise with an angle of ϕ in comparison to the incident beam. The corresponding electric field can be expressed as follows:

$$E = ie^{-i\phi} \begin{bmatrix} 1 \\ i \end{bmatrix} + ie^{i\phi} \begin{bmatrix} 1 \\ -i \end{bmatrix} = i \begin{bmatrix} \cos\phi \\ \sin\phi \end{bmatrix}. \tag{A4}$$

When an additional phase of $\varphi_{\mathrm{RCP}} = -\left\{\frac{2\pi}{\lambda} \cdot \left[\sqrt{(x-x_R)^2 + (y-y_R)^2 + f_R^2} - f_R\right] + l_R\varphi\right\}$ is embedded into the designed geometric metasurface, the incident RCP beam can be focused and modulated into an LCP converged vortex. Therefore, the Jones vector of the converted beam under the illumination of an LP beam can be written as

$$\begin{aligned} &\frac{1}{\sqrt{2}} \left\{ \frac{1}{\sqrt{2}} \begin{bmatrix} 1 \\ i \end{bmatrix} \exp(-i\phi) \exp\left[i\varphi_{\mathrm{RCP}}(x,y)\right] \right. \\ &\left. + \frac{1}{\sqrt{2}} \begin{bmatrix} 1 \\ -i \end{bmatrix} \exp(i\phi) \exp\left[-i\varphi_{\mathrm{RCP}}(x,y)\right] \right\}. \end{aligned} \tag{A5}$$

If an opposite phase of $\varphi_{\mathrm{LCP}} = \frac{2\pi}{\lambda} \cdot \left[\sqrt{(x-x_L)^2 + (y-y_L)^2 + f_L^2} - f_L\right] + l_L\varphi$ is introduced into a geometric metasurface (under illumination of an LP beam), the corresponding Jones vector of the converted beam is described as

$$\begin{aligned} &\frac{1}{\sqrt{2}} \left\{ \frac{1}{\sqrt{2}} \begin{bmatrix} 1 \\ i \end{bmatrix} \exp(-i\phi) \exp\left[i\varphi_{\mathrm{LCP}}(x,y)\right] \right. \\ &\left. + \frac{1}{\sqrt{2}} \begin{bmatrix} 1 \\ -i \end{bmatrix} \exp(i\phi) \exp\left[-i\varphi_{\mathrm{LCP}}(x,y)\right] \right\}. \end{aligned} \tag{A6}$$

To obtain an LP converged vortex with polarization-rotatable functionality, both $\varphi_{\mathrm{RCP}}(x,y)$ and $\varphi_{\mathrm{LCP}}(x,y)$ should be simultaneously embedded into a geometric metasurface, and

the Jones vector of the transmitted waves is the superposition of Eqs. (A5) and (A6):

$$\frac{1}{\sqrt{2}}\left\{\frac{1}{\sqrt{2}}\begin{bmatrix}1\\ i\end{bmatrix}\exp(-i\phi)\exp\left[i\varphi_{\mathrm{RCP}}(x,y)\right] + \frac{1}{\sqrt{2}}\begin{bmatrix}1\\ -i\end{bmatrix}\exp(i\phi)\exp\left[-i\varphi_{\mathrm{RCP}}(x,y)\right]\right\} + \frac{1}{\sqrt{2}}\left\{\frac{1}{\sqrt{2}}\begin{bmatrix}1\\ i\end{bmatrix}\exp(-i\phi)\exp\left[i\varphi_{\mathrm{LCP}}(x,y)\right] + \frac{1}{\sqrt{2}}\begin{bmatrix}1\\ -i\end{bmatrix}\exp(i\phi)\exp\left[-i\varphi_{\mathrm{LCP}}(x,y)\right]\right\}. \tag{A7}$$

The above equation can also be written as

$$\exp(i\varphi_{\mathrm{RCP}})\begin{bmatrix}\cos\phi\\ \sin\phi\end{bmatrix} + \exp(i\varphi_{\mathrm{LCP}})\begin{bmatrix}\cos\phi\\ \sin\phi\end{bmatrix}. \tag{A8}$$

Therefore, the required phase distribution for the designed metasurface to generate converged vortices with polarization-rotatable functionality is governed by

$$\Phi_2 = \arg\left\{\exp\left[i(\phi+\varphi_{\mathrm{LCP}})\right] + \exp\left[i(\phi+\varphi_{\mathrm{RCP}})\right]\right\}. \tag{A9}$$

Furthermore, we can integrate a variety of converged vortices with different orientations of LP states into a single metasurfce to demonstrate the multiplexing of polarization-rotatable multiple vortices in multiple spatial dimensions. The corresponding phase profile of the geometric metasurface can be written as

$$\Phi_3 = \arg\left\{\sum_{i=1}^{N}\left[A_i\exp(i\varphi_{i\text{-LCP}}) + B_i\exp(i\varphi_{i\text{-RCP}})\right]\right\}, \tag{A10}$$

where $\varphi_{i\text{-LCP}} = \left\{\frac{2\pi}{\lambda}\left[\sqrt{(x-x_{i\text{-}L})^2+(y-y_{i\text{-}L})^2+f_{i\text{-}L}^2}-f_{i\text{-}L}\right]+l_{i\text{-}L}\varphi\right\}+\phi_i$ and $\varphi_{i\text{-RCP}} = -\left\{\frac{2\pi}{\lambda}\left[\sqrt{(x-x_{i\text{-}R})^2+(y-y_{i\text{-}R})^2+f_{i\text{-}R}^2}-f_{i\text{-}R}\right]+l_{i\text{-}R}\varphi\right\}+\phi_i$, $i = 1, 2, 3, \ldots$, and $f_{i\text{-}L} = f_{i\text{-}R}$, $x_{i\text{-}L} = x_{i\text{-}R}$, $y_{i\text{-}L} = y_{i\text{-}R}$, $l_{i\text{-}L} = l_{i\text{-}R}$. If the ith LP vortex with polarization-rotatable functionality is required to be generated after the metasurface, the phase parameters are $A_i = B_i = 1$, and ϕ_i is the corresponding polarization-rotation angle. Accordingly, if it is the ith vortex with LCP/RCP state, the phase parameters are $A_i = 1$, $B_i = 0$ (or $A_i = 0$, $B_i = 1$).

APPENDIX B: ELECTRIC-FIELD INTENSITY DISTRIBUTION OF POLARIZATION-INDEPENDENT CONVERGED VORTEX IN THE *X–Z* PLANE

Figure 8 shows the numerical simulations and experimental demonstration of the electric-field intensity distributions in the x–z plane for the polarization-independent (converged) vortex with $l_L = l_R = 1$. As depicted in Figs. 8(a_1)–8(b_5), each electric-field intensity distribution under the illumination of an arbitrarily polarized THz wave shows a similar characteristic. The focal plane for the simulated and measured results is nearly located at $z = 7.5$ mm. The main electric-field intensity distributions of the numerical calculations range from 6.5 mm to 8.7 mm, while they are located between 5.5 mm and 9.5 mm in experiments. Both the calculated and measured electric-field intensity distributions demonstrate that the designed geometric metasurface [see Fig. 2(c)] enables the polarization-independent functionality.

APPENDIX C: MULTIPLEXING OF POLARIZATION-ROTATABLE CONVERGED VORTICES

1. Polarization-Rotatable Vortex

Figure 9 shows the electric-field intensity and phase distributions of the designed geometric metasurface that can generate a polarization-rotatable (converged) vortex. Under the illumination of x-polarized THz waves, a converged vortex with the y-polarized state and focal length of $z = 7.5$ mm is generated after the metasurface for $\phi = 90°$ [see Fig. 9(a2)] and none of the x-polarized converged vortex can be observed [see Fig. 9(a_1)], demonstrating an LP converged vortex with polarization-rotatable functionality. The phase distribution shown in Fig. 9(a_3) indicates that the topological charge of the converged vortex is one. The measured electric-field intensity and phase distributions are shown in Figs. 9(b_1)–9(b_3). A y-polarized converged vortex with a corresponding focal length of $z = 7.5$ mm is also observed after the fabricated sample [see Fig. 9(b_2)]. The calculated and measured electric-field distributions in the x–z plane [see Figs. 9(a_4)–9(b_5)] also demonstrate that our proposed approach enables the functionality for generating a polarization-rotatable converged vortex.

2. Multiplexing of LP Converged Vortices in Transverse Direction

Figure 10 shows the multiplexing of two symmetrically distributed LP converged vortices in the transverse direction. Parameters of the phase profile are selected as $x_{1\text{-}L} = x_{1\text{-}R} = -x_{2\text{-}L} = -x_{2\text{-}R} = -2$ mm, $y_{1\text{-}L} = y_{1\text{-}R} = y_{2\text{-}L} = y_{2\text{-}R} = 0$, $l_{1\text{-}L} = l_{1\text{-}R} = l_{2\text{-}L} = l_{2\text{-}R} = 1$, $f_{1\text{-}L} = f_{1\text{-}R} = f_{2\text{-}L} = f_{2\text{-}R} = 8$ mm, $\phi_1 = 0$, and $\phi_2 = \frac{\pi}{2}$. For the incidence of x-polarized terahertz waves, two converged vortices with different orientations of polarizations will be generated. The calculated results are shown in Figs. 10(a_1) and 10(b_1), and the x- and y-polarized (converged) vortices are located at (–2 mm, 0, 7.5 mm) and (2 mm, 0, 7.5 mm), respectively. Figures 10(a_2) and 10(b_2) are the corresponding phase distributions, which show that the topological charge of each vortex is one. The electric-field intensity distributions in the x–z plane [see Figs. 10(c_1) and 10(c_2)] also demonstrate that two converged vortices with orthogonal LP states are observed. The measured electric-field intensity and phase distributions in the x–y and x–z planes are shown in Figs. 10(a_3)–10(c_3) and Figs. 10(a_4)–10(c_4), respectively. The measured results match well with the numerical simulations.

3. Multiplexing of CP Converged Vortices in Longitudinal Direction

In addition to the transverse and longitudinal multiplexing of LP converged vortices, the multiplexing of CP converged vortices in the longitudinal (or transverse) direction can also be realized based on our proposed approach. For longitudinal multiplexing of a CP wave, we select phase profile parameters as $x_L = x_R = y_L = y_R = 0$, $l_L = l_R = 1$, and $f_L = 4.5$ mm, $f_R = 8.5$ mm. For the incidence of LCP THz waves, one

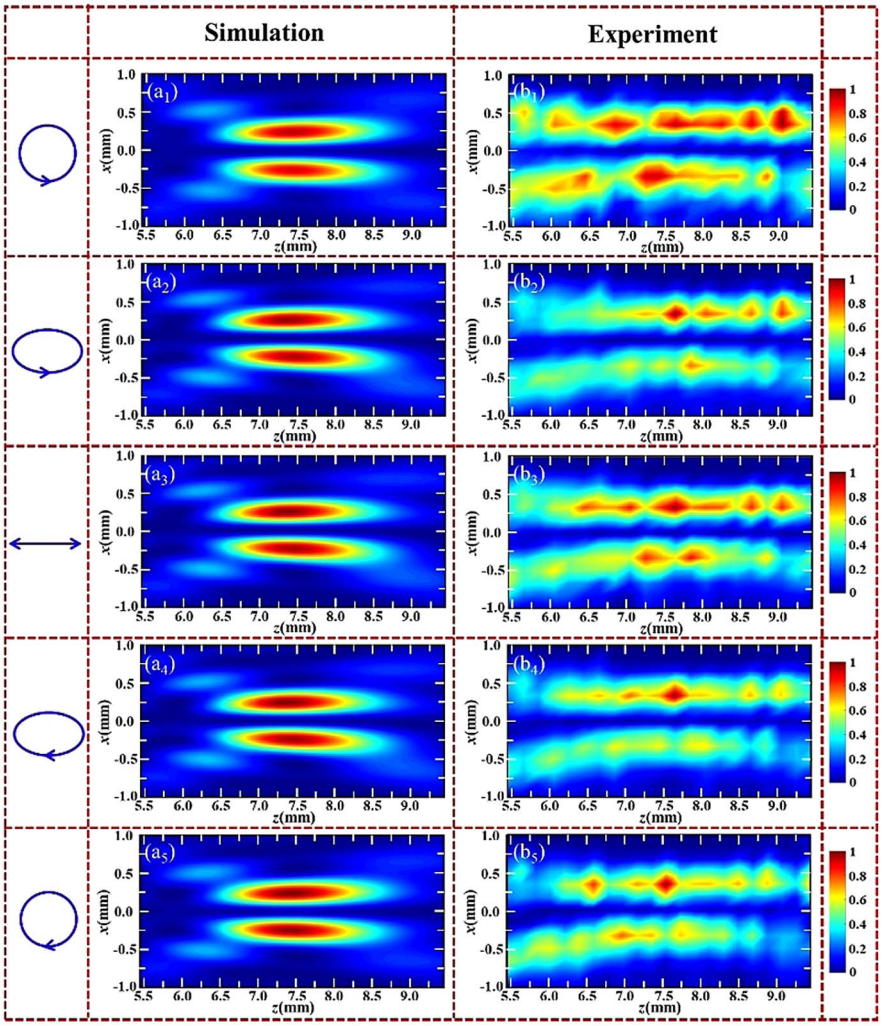

Fig. 8. Electric-field intensity distributions of spin-independent vortices in the x–z plane. (a_1)–(a_5) Simulated electric-field intensity distributions for the designed geometric metasurface under illumination of LCP, LECP, LP, RECP, and RCP THz waves in the x–z plane. (b_1)–(b_5) Measured electric-field intensity distributions of the corresponding vortices.

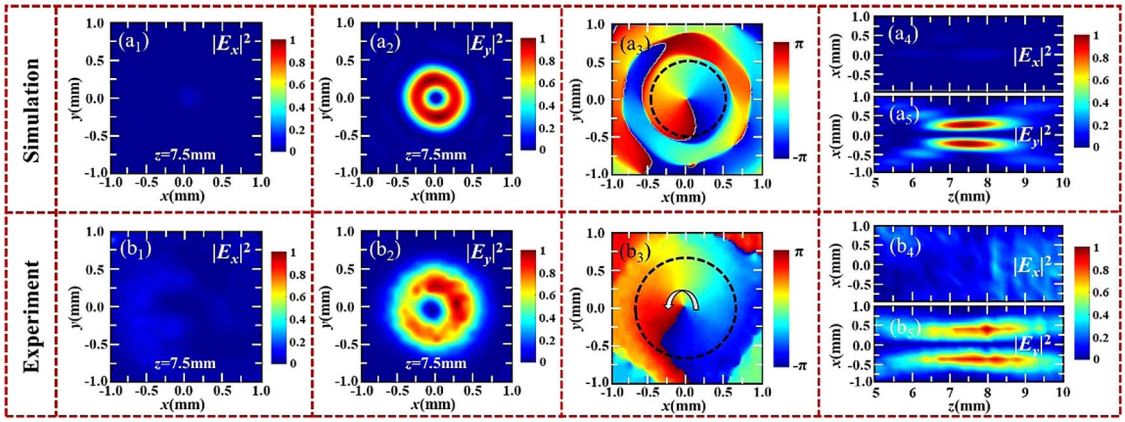

Fig. 9. Electric-field intensity and phase distributions for the polarization-rotatable vortex ($l = 1$) under illumination of LP THz waves. (a_1), (a_2) Simulated x- and y-polarized electric-field intensity distributions at $z = 7.5$ mm. (b_1), (b_2) Measured electric-field intensity distributions for (a_1) and (a_2). (a_3), (b_3) Simulated and measured phase distributions for the y-polarized converged vortex at $z = 7.5$ mm. (a_4), (a_5) Simulated electric-field intensity distributions for $|E_x|^2$ and $|E_y|^2$ in the x–z plane. (b_4), (b_5) Measured results for (a_4) and (a_5).

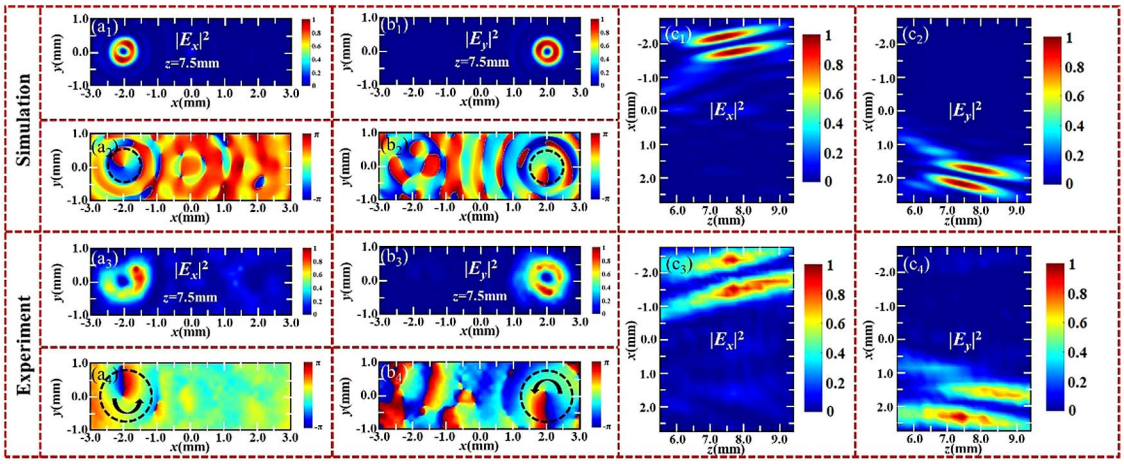

Fig. 10. Electric-field intensity and phase distributions of the multiplexing of two vortices with two orthogonal LP states in the transverse direction. (a_1)–(a_4) Simulated and measured electric-field intensity and phase distributions for $|E_x|^2$ at $z = 7.5$ mm. (b_1)–(b_4) Simulated x- and y-polarized phase distributions at $z = 7.5$ mm. (c_1), (c_2) Simulated electric-field distributions for $|E_x|^2$ and $|E_y|^2$ in the x–z plane. (c_3), (c_4) Measured electric-field intensity distribution in the x–z plane.

converged vortex with a topological charge of one is observed at a focal plane of $z = 4.3$ mm, as shown in Figs. 11(a_1) and 11(a_3). In addition, another converged vortex with a topological charge of one can be observed in the focal plane of $z = 7.9$ mm for the incidence of RCP THz waves [see Figs. 11(a_2) and 11(a_4)]. The corresponding electric-field intensity distributions for the incidence of LCP and RCP THz waves are shown in Figs. 11(a_5) and 11(a_6), respectively. Under illumination of an LP THz beam, two coaxially distributed converged vortices are simultaneously observed after the designed metasurface. Figures 11(b_1)–11(b_7) show the experimental demonstration of the multiplexing of CP converged vortices in the longitudinal direction. The measured results agree well with the numerical simulations.

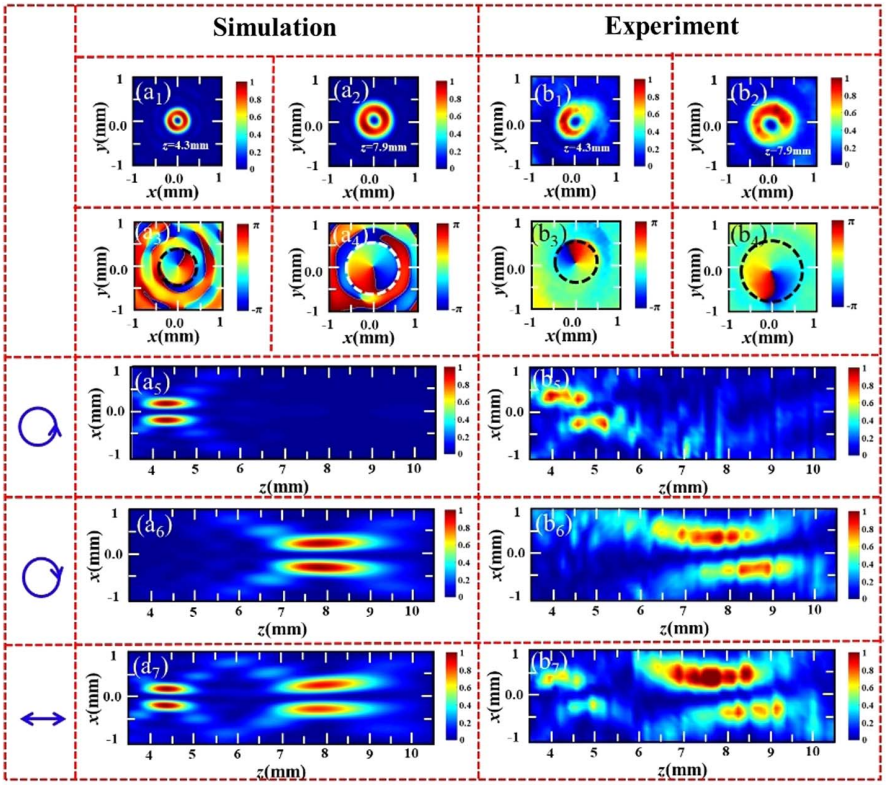

Fig. 11. Electric-field intensity and phase distributions of the multiplexing of two vortices with two orthogonal helical states in the longitudinal direction. (a_1)–(b_2) Simulated and measured electric-field intensity distributions at $z = 4.3$ mm and $z = 7.9$ mm, respectively. (a_3)–(b_4) Corresponding phase distributions for (a_1)–(b_2). (a_5)–(b_7) Simulated and measured electric-field intensity distributions in the x–z plane.

4. Multiplexing of CP Converged Vortices in Transverse Direction

The proposed approach can also be extended to design a geometric metasurface that can further realize the multiplexing of CP converged vortices in the transverse direction (see Fig. 12). Parameters of the phase profile are selected as $x_L = -x_R = -2$, $y_L = y_R = 0$, $l_L = l_R = 1$, and $f_L = 4.5$ mm, $f_R = 8.5$ mm. For the incidence of LCP THz waves, a converged vortex located at (−2.0 mm, 0, 7.5 mm) is observed, while another converged vortex located at (−2.0 mm, 0, 7.5 mm) is generated under the illumination of RCP THz waves [see Figs. 12(a_1) and 12(a_3)]. The topological charge of each vortex is one, as shown in Figs. 12(a_2) and 12(a_4). The electric-field intensity distributions in the x–z plane are shown in Figs 12(c_1) and 12(c_3), and they also demonstrate two helicity-dependent (converged) vortices (under illumination of LCP/RCP THz waves). For the incidence of LP THz waves, two converged vortices with identical topological charges of one are simultaneously observed [see Figs. 12(a_5) and 12(a_6)]. The corresponding demonstrations in experiment are shown in Figs. 12(b_1)–12(b_6) and Figs. 12(c_2), 12(c_4), and 12(c_6), which match with the numerical calculations.

APPENDIX D: ELECTRIC-FIELD INTENSITY DISTRIBUTIONS OF THE MULTIPLEXING OF CONVERGED VORTICES WITH MULTIPLE POLARIZATION STATES

To demonstrate the versatility of our proposed approach, we further study the multiplexing of converged vortices with both CP and LP states. The designed parameters of the phase profile are $x_{1\text{-}L} = x_{1\text{-}R} = -x_{2\text{-}L} = -x_{2\text{-}R} = -2$ mm, $x_{3\text{-}L} = x_{3\text{-}R} = 0$, $\phi_1 = 0$, $\phi_2 = \frac{\pi}{2}$, $\phi_3 = 0$, $y_{1\text{-}L} = y_{1\text{-}R} = y_{2\text{-}L} = y_{2\text{-}R} = y_{3\text{-}L} = y_{3\text{-}R} = 0$, $l_{1\text{-}L} = l_{1\text{-}R} = l_{2\text{-}L} = l_{2\text{-}R} = l_{3\text{-}L} = l_{3\text{-}R} = 1$, $f_{1\text{-}L} = f_{1\text{-}R} = f_{2\text{-}L} = f_{2\text{-}R} = 6.5$ mm, $f_{3\text{-}L} = f_{3\text{-}R} = 8.5$ mm. Under illumination of x-polarized THz waves, two LP converged vortices and one CP converged vortex are generated: one x-polarized converged vortex located at (−2.0 mm, 0, 6.3 mm), one y-polarized (converged) vortex located at (−2.0 mm, 0, 6.3 mm), and one RCP converged vortex located at (0, 0, 7.9 mm) [see Figs. 13(a_1)–13(b_8)]. The electric-field intensities for $|E_x|^2$, $|E_y|^2$, and $|E_x|^2 + |E_y|^2$ in the x–z plane are shown in Figs. 13(a_9)–13(b_{11}), which also demonstrates that two LP (converged) vortices and one CP (converged) vortex are observed.

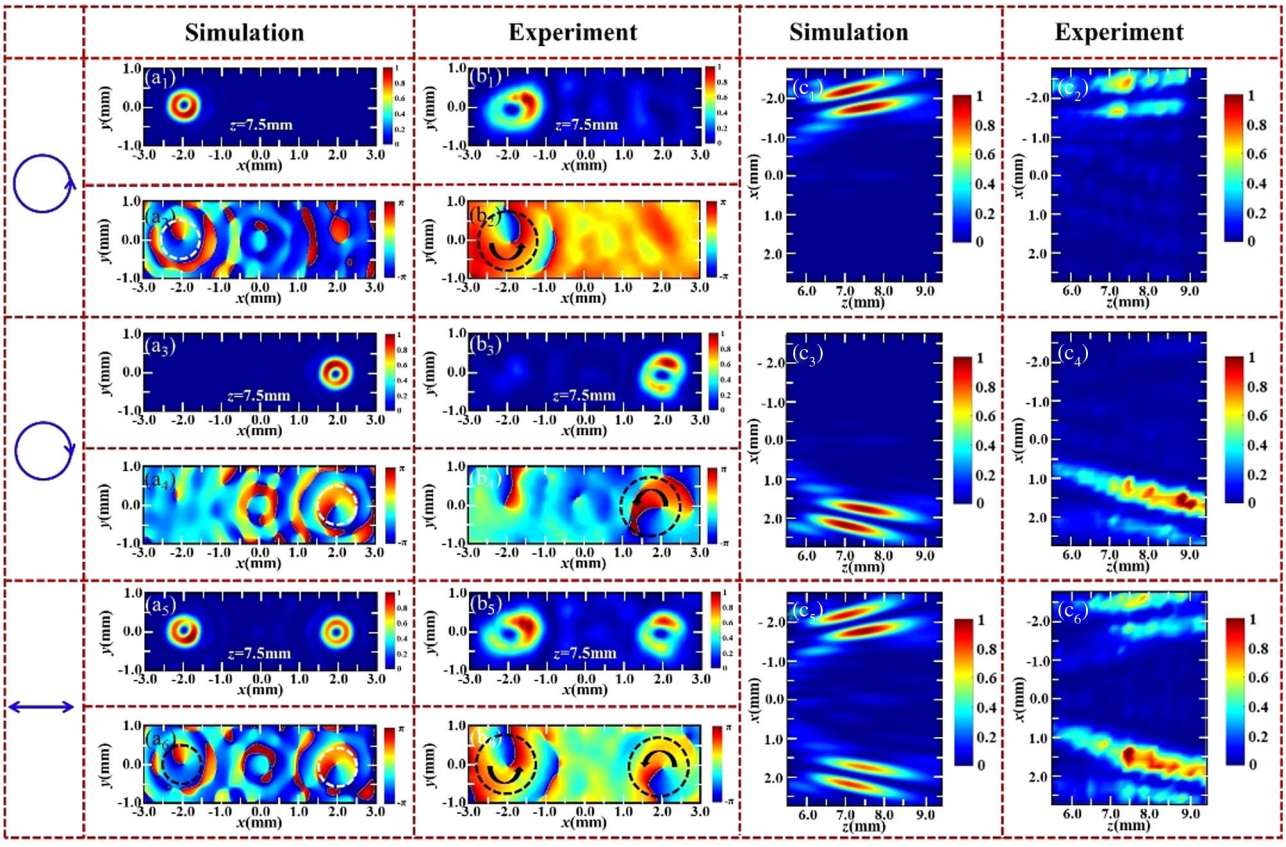

Fig. 12. Electric-field intensity and phase distributions of the multiplexing of two vortices with two orthogonal helical states in the transverse direction. (a_1)–(b_6) Simulated and measured electric-field intensity and phase distributions at $z = 7.5$ mm, under the illumination of LCP (a_1)–(b_2), RCP (a_3)–(b_4), and LP (a_5)–(b_6) THz waves. (c_1)–(c_6) Simulated and measured electric-field intensity distributions in the x–z plane.

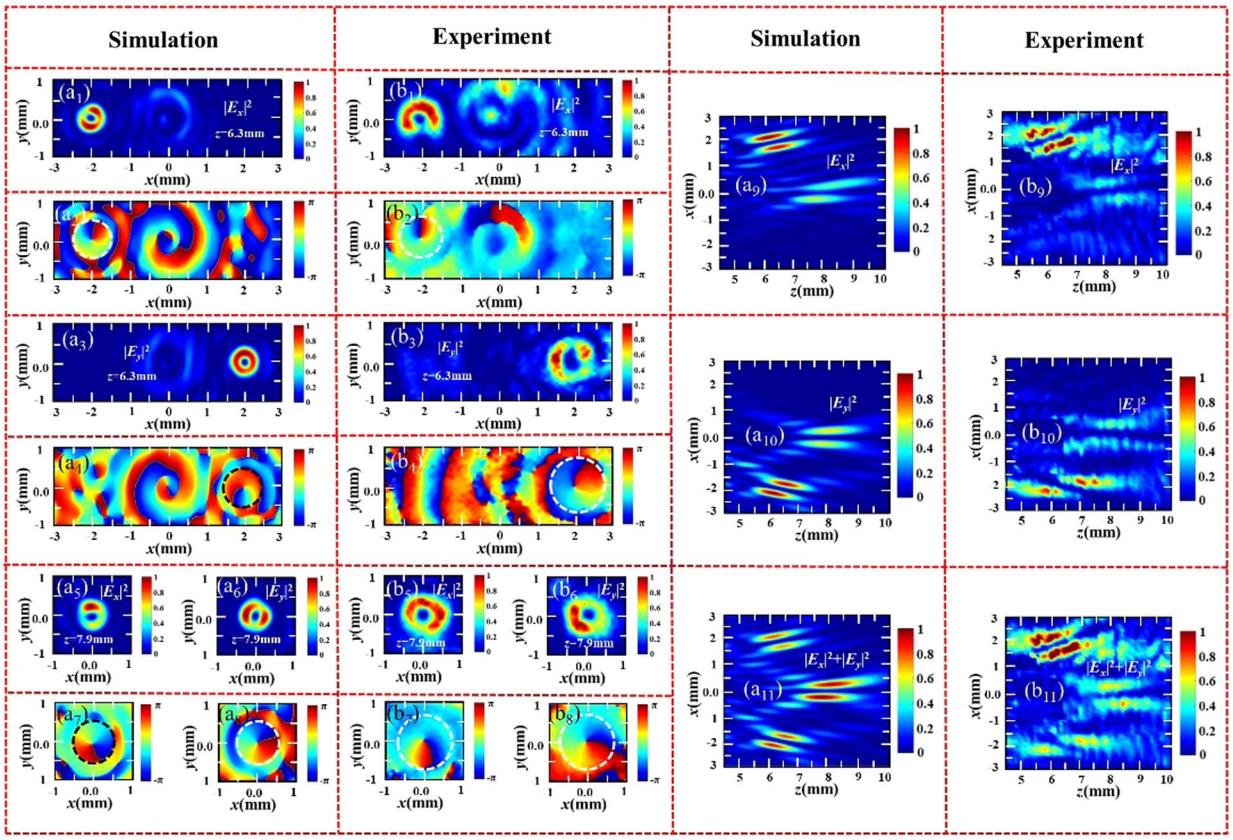

Fig. 13. Electric-field intensity and phase distributions of the multiplexing of three vortices with LP states and CP state. (a_1)–(b_8) Simulated and measured electric-field intensity and phase distributions at $z = 6.3$ mm and $z = 7.9$ mm, respectively. (a_9)–(b_{11}) Simulated and measured electric-field intensity distributions in the x–z plane.

APPENDIX E: ELECTRIC-FIELD INTENSITY DISTRIBUTIONS OF THE MULTIPLEXING OF CONVERGED VORTICES WITH DIFFERENT TOPOLOGICAL CHARGES

Figures 14(a_1)–14(a_6) show the electric-field intensity and phase distributions of a geometric metasurface that can generate two vortices with orthogonal CP states and different topological charges. The phase profile for the geometric metasurface is governed by $\Phi_{CP} = \arg[\exp(i\varphi_{LCP}) + \exp(i\varphi_{RCP})]$, where $\varphi_{LCP} = \frac{2\pi}{\lambda}(\sqrt{x^2+y^2+f_L^2}-f_L)+l_L\varphi$ and $\varphi_{RCP}=-\frac{2\pi}{\lambda}(\sqrt{x^2+y^2+f_R^2}-f_R)-l_R\varphi$. Parameters for these two helical phases are given as $f_L = 4.5$ mm, $f_R = 8.5$ mm, $l_L = 3$, and $l_R = 1$. For the incidence of LCP THz waves, an RCP converged vortex is observed at the focal plane with $z = 4.3$ mm [see Figs. 14(a_1) and 14(a_5)], while an LCP converged vortex can be generated at $z = 7.9$ mm under illumination of RCP THz waves [see Figs. 14(a_2) and 14(a_6)]. The phase changes (around the singular point) for RCP and LCP converged vortices are 6π and 2π, which means that the corresponding topological charges are three and one, respectively [see Figs. 14(a_3) and 14(a_4)].

According to the aforementioned approach, the generation of two (or multiple) vortices with orthogonal LP states and different topological charges can also be realized by the superposition of two orthogonal helical vortices with identical topological charges. The phase profile for the geometric metasurface can be illustrated as $\Phi_{LP}=\arg[\exp(i\varphi_{1\_LCP})+\exp(i\varphi_{1\_RCP})+\exp(i\varphi_{2\_LCP})+\exp(i\varphi_{2\_RCP})]$, where $\varphi_{1\_LCP} = \frac{2\pi}{\lambda}\left(\sqrt{x^2+y^2+f_{1\_L}^2}-f_{1\_L}\right)+l_{1\_L}\varphi$, $\varphi_{1\_RCP} = -\frac{2\pi}{\lambda}\cdot\left(\sqrt{x^2+y^2+f_{1\_R}^2}-f_{1\_R}\right)+l_{1\_R}\varphi$, $\varphi_{2\_LCP} = \frac{2\pi}{\lambda}\cdot\left(\sqrt{x^2+y^2+f_{2\_L}^2}-f_{2\_L}\right)+l_{2\_L}\varphi+\phi$, and $\varphi_{RCP\_2} = -\frac{2\pi}{\lambda}\left(\sqrt{x^2+y^2+f_{R\_2}^2}-f_{R\_2}\right)+l_{R\_2}\varphi+\phi$ ($\phi = 90°$). The corresponding parameters for these four helical phases are given as $f_{1\_L} = f_{1\_R} = 4.5$ mm, $f_{2\_L} = f_{2\_R} = 8.5$ mm, $l_{1\_L} = l_{1\_R} = 3$, and $l_{2\_L} = l_{2\_R} = -2$. Under illumination of x-polarized THz waves, one x-polarized and converged vortex is observed at the focal plane with $z = 4.3$ mm [see Figs. 14(b_1) and 14(b_5)], while another x-polarized and converged vortex is generated at the focal plane with $z = 7.9$ mm [see Figs. 14(b_2) and 14(b_6)]. The topological charges for these two converged vortices with orthogonal LP states are 3 and –2, respectively [see Figs. 14(b_3) and 14(b_4)].

APPENDIX F: PHASE DISTRIBUTIONS FOR EXTENDED FOCAL DEPTH OF CONVERGED VORTEX

The calculated and measured phase distributions of the E_x and E_y components for the generated vortices are shown in Fig. 15.

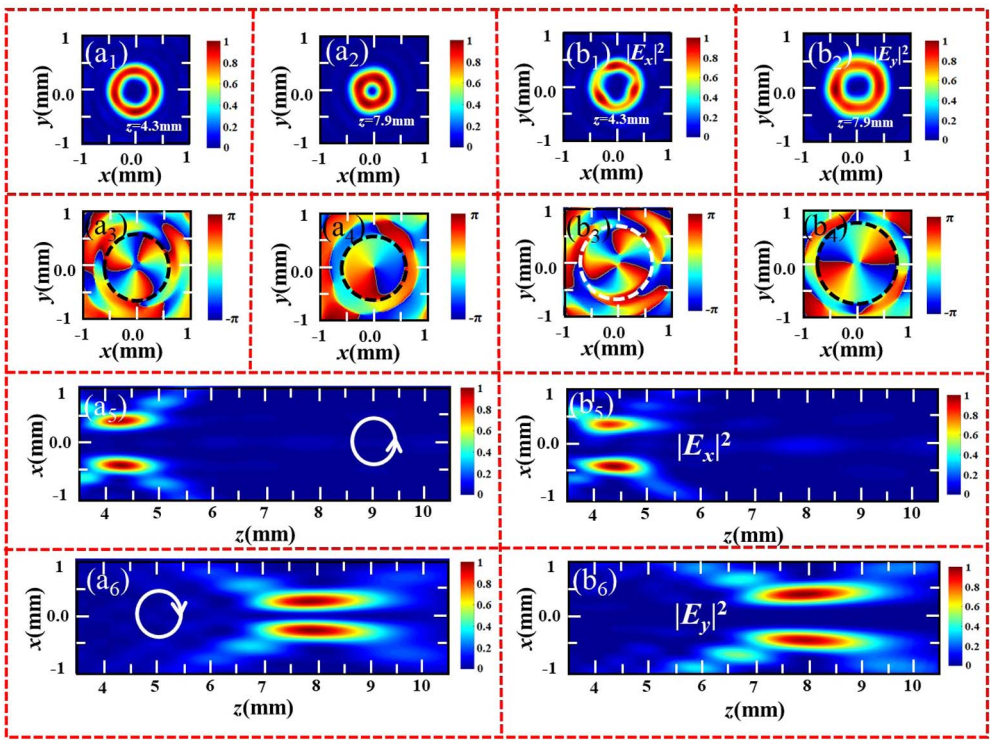

Fig. 14. Electric-field intensity and phase distributions of the multiplexing of two vortices with two orthogonal CP (a_1)–(a_6) or LP (b_1)–(b_6) states in the longitudinal direction. (a_1), (a_2) Simulated and measured electric-field intensity distributions at $z = 4.3$ mm and $z = 7.9$ mm, respectively. (a_3), (a_4) Corresponding phase distributions for (a_1), (a_2). (a_5), (a_6) Simulated and measured electric-field intensity distributions in the x–z plane. (b_1), (b_2) Simulated and measured electric-field intensity distributions at $z = 4.3$ mm and $z = 7.9$ mm, respectively. (b_3), (b_4) Corresponding phase distributions for (b_1), (b_2). (b_5), (b_6) Simulated and measured electric-field intensity distributions in the x–z plane.

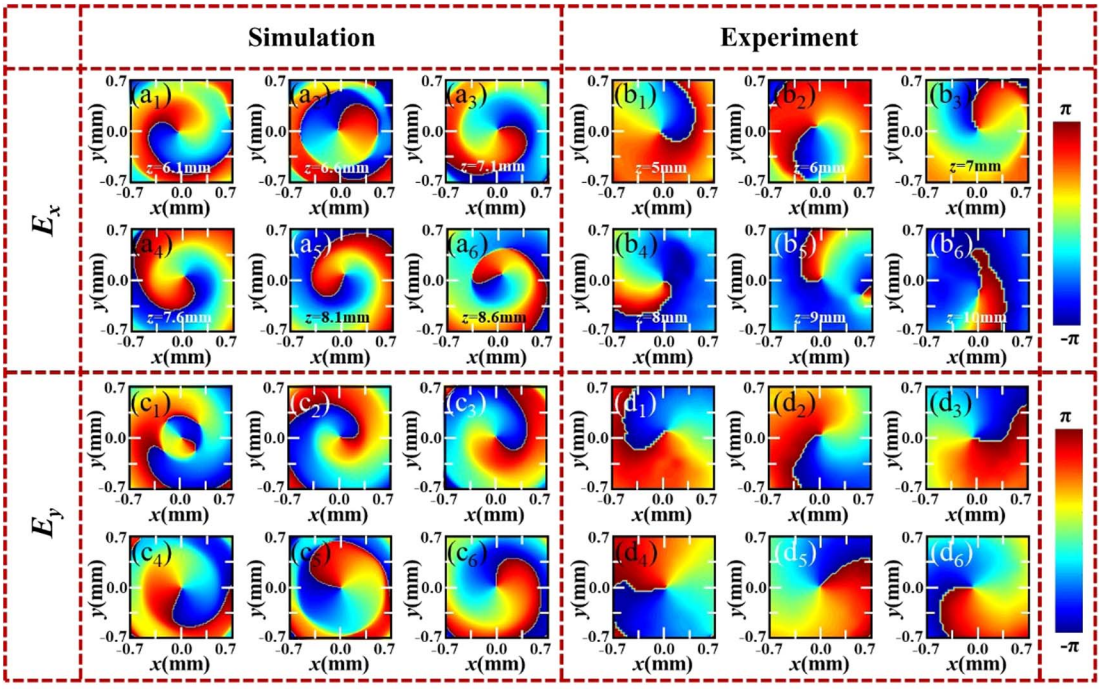

Fig. 15. Phase distributions of a vortex with extended focal length. (a_1)–(a_6), (b_1)–(b_6) Simulated and measured phase distributions for x component in different x–y planes. (c_1)–(c_6), (d_1)–(d_6) Simulated and measured phase distributions for y component in different x–y planes.

The phase distributions at different x–y planes illustrate that both the x-polarized and y-polarized converged vortices enable the identical topological charge of one. The helical phase in each x–y plane is rotated clockwise away from the metasurface.

Funding. National Key Research and Development Program of China (2017YFA0701005); National Natural Science Foundation of China (61722111, 61871268); "Shuguang" Program of Shanghai Education Commission (19SG44); Program of General Administration of Customs of the People's Republic of China (2019HK006); Shanghai International Joint Laboratory Project (17590750300); 111 Project (D18014); Interdisciplinary Scientific and Educational School of Moscow University "Photonic and Quantum Technologies. Digital Medicine".

Disclosures. The authors declare no conflicts of interest.

Data Availability. The data that support the findings of this study are available from the corresponding author upon reasonable request.

REFERENCES

1. L. Allen, M. W. Beijersbergen, R. J. Spreeuw, and J. P. Woerdman, "Orbital angular momentum of light and the transformation of Laguerre-Gaussian laser modes," Phys. Rev. A **45**, 8185–8189 (1992).
2. F. Gori, "Polarization basis for vortex beams," J. Opt. Soc. Am. A **18**, 1612–1617 (2001).
3. Q. Zhan, "Cylindrical vector beams: from mathematical concepts to applications," Adv. Opt. Photon. **1**, 1–57 (2009).
4. J. Wang, J.-Y. Yang, I. M. Fazal, N. Ahmed, Y. Yan, H. Huang, Y. Ren, Y. Yue, S. Dolinar, M. Tur, and A. E. Willner, "Terabit free-space data transmission employing orbital angular momentum multiplexing," Nat. Photonics **6**, 488–496 (2012).
5. Y. Yan, G. Xie, M. P. Lavery, H. Huang, N. Ahmed, C. Bao, Y. Ren, Y. Cao, L. Li, Z. Zhao, A. F. Molisch, M. Tur, M. J. Padgett, and A. E. Willner, "High-capacity millimetre-wave communications with orbital angular momentum multiplexing," Nat. Commun. **5**, 4876 (2014).
6. K. Sueda, G. Miyaji, N. Miyanaga, and M. Nakatsuka, "Laguerre-Gaussian beam generated with a multilevel spiral phase plate for high intensity laser pulses," Opt. Express. **12**, 3548–3553 (2004).
7. E. Karimi, B. Piccirillo, E. Nagali, L. Marrucci, and E. Santamato, "Efficient generation and sorting of orbital angular momentum eigenmodes of light by thermally tuned q-plates," Appl. Phys. Lett. **94**, 231124 (2009).
8. M. W. Beijersbergen, L. Allen, H. E. L. O. van der Veen, and J. P. Woerdman, "Astigmatic laser mode converters and transfer of orbital angular momentum," Opt. Commun. **96**, 123–132 (1993).
9. A. S. Ostrovsky, C. Rickenstorff-Parrao, and V. Arrizón, "Generation of the "perfect" optical vortex using a liquid-crystal spatial light modulator," Opt. Lett. **38**, 534–536 (2013).
10. N. F. Yu, P. Genevet, M. A. Kats, F. Aieta, J. P. Tetienne, F. Capasso, and Z. Gaburro, "Light propagation with phase discontinuities: generalized laws of reflection and refraction," Science **334**, 333–337 (2011).
11. L. L. Huang, X. Z. Chen, H. Muhlenbernd, G. X. Li, B. F. Bai, Q. F. Tan, G. F. Jin, T. Zentgraf, and S. Zhang, "Dispersionless phase discontinuities for controlling light propagation," Nano Lett. **12**, 5750–5755 (2012).
12. X. Chen, L. Huang, H. Mühlenbernd, G. Li, B. Bai, Q. Tan, G. Jin, C. Qiu, S. Zhang, and T. Zentgraf, "Dual-polarity plasmonic metalens for visible light," Nat. Commun. **3**, 1198 (2012).
13. A. Arbabi, Y. Horie, A. J. Ball, M. Bagheri, and A. Faraon, "Subwavelength-thick lenses with high numerical apertures and large efficiency based on high-contrast transmitarrays," Nat. Commun. **6**, 7069 (2015).
14. M. Khorasaninejad, W. T. Chen, R. C. Devlin, J. Oh, A. Y. Zhu, and F. Capasso, "Metalenses at visible wavelengths: diffraction-limited focusing and subwavelength resolution imaging," Science **352**, 1190–1194 (2016).
15. S. Wang, P. C. Wu, V. C. Su, Y. C. Lai, C. H. Chu, J. W. Chen, S. H. Lu, J. Chen, B. Xu, C. H. Kuan, T. Li, S. N. Zhu, and D. P. Tsai, "Broadband achromatic optical metasurface devices," Nat. Commun. **8**, 187 (2017).
16. W. T. Chen, A. Y. Zhu, V. Sanjeev, M. Khorasaninejad, Z. J. Shi, E. Lee, and F. Capasso, "A broadband achromatic metalens for focusing and imaging in the visible," Nat. Nanotechnol. **13**, 220–226 (2019).
17. R. J. Lin, V.-C. Su, S. Wang, M. K. Chen, T. L. Chung, Y. H. Chen, H. Y. Kuo, J.-W. Chen, J. Chen, Y.-T. Huang, J.-H. Wang, C. H. Chu, P. C. Wu, T. Li, Z. Wang, S. Zhu, and D. P. Tsai, "Achromatic metalens array for full-colour light-field imaging," Nat. Nanotechnol. **14**, 227–231 (2019).
18. Y. Wang, Q. Chen, W. Yang, Z. Ji, L. Jin, X. Ma, Q. Song, A. Boltasseva, J. Han, V. M. Shalaev, and S. Xiao, "High-efficiency broadband achromatic metalens for near-IR biological imaging window," Nat. Commun. **12**, 5560 (2021).
19. N. Yu, F. Aieta, P. Genevet, M. A. Kats, Z. Gaburro, and F. Capasso, "A broadband, background-free quarter-wave plate based on plasmonic metasurfaces," Nano Lett. **12**, 6328–6333 (2012).
20. N. K. Grady, J. E. Heyes, D. R. Chowdhury, Y. Zeng, M. T. Reiten, A. K. Azad, A. J. Taylor, D. A. Dalvit, and H. T. Chen, "Terahertz metamaterials for linear polarization conversion and anomalous refraction," Science **340**, 1304–1307 (2013).
21. P. C. Wu, W. Y. Tsai, W. T. Chen, Y. W. Huang, T. Y. Chen, J. W. Chen, C. Y. Liao, C. H. Chu, G. Sun, and D. P. Tsai, "Versatile polarization generation with an aluminum plasmonic metasurface," Nano Lett. **17**, 445–452 (2017).
22. D. D. Wen, F. Y. Yue, C. M. Zhang, X. F. Zang, H. G. Liu, W. Wang, and X. Z. Chen, "Plasmonic metasurface for optical rotation," Appl. Phys. Lett. **111**, 023102 (2017).
23. X. F. Zang, F. L. Dong, F. Y. Yue, C. M. Zhang, L. Xu, Z. Song, M. Chen, P. Y. Chen, G. S. Buller, Y. M. Zhu, S. L. Zhuang, W. G. Chu, S. Zhang, and X. Z. Chen, "Polarization encoded color image embedded in a dielectric metasurface," Adv. Mater. **30**, 1707499 (2018).
24. X. F. Zang, H. H. Gong, Z. Li, J. Y. Xie, Q. Q. Cheng, L. Chen, A. P. Shkurinov, Y. M. Zhu, and S. L. Zhuang, "Metasurface for multichannel terahertz beam splitters and polarization rotators," Appl. Phys. Lett. **112**, 171111 (2018).
25. A. H. Dorrah, N. A. Rubin, A. Zaidi, M. Tamagnone, and F. Capasso, "Metasurface optics for on-demand polarization transformations along the optical path," Nat. Photonics **15**, 287–296 (2021).
26. L. Q. Cong, N. N. Xu, J. G. Han, W. L. Zhang, and R. Singh, "A tunable dispersion-free terahertz metadevice with Pancharatnam-Berry-phase-enabled modulation and polarization control," Adv. Mater. **27**, 6630–6636 (2015).
27. L. Q. Cong, N. N. Xu, J. Q. Gu, R. Singh, J. G. Han, and W. L. Zhang, "Highly flexible broadband terahertz metamaterial quarter-wave plate," Laser Photon. Rev. **8**, 626–632 (2015).
28. L. Q. Cong, W. Cao, X. Q. Zhang, Z. Tian, J. Q. Gu, R. Singh, J. G. Han, and W. L. Zhang, "A perfect metamaterial polarization rotator," Appl. Phys. Lett. **103**, 171107 (2013).
29. X. B. Yin, Z. L. Ye, J. Rho, Y. Wang, and X. Zhang, "Photonic spin Hall effect at metasurfaces," Science **339**, 1405–1407 (2013).
30. X. H. Ling, X. X. Zhou, X. N. Yi, W. X. Shu, Y. C. Liu, S. Z. Chen, H. L. Luo, S. C. Wen, and D. Y. Fan, "Giant photonic spin Hall effect in momentum space in a structured metamaterial with spatially varying birefringence," Light Sci. Appl. **4**, e290 (2015).
31. J. Zhou, H. Qian, G. Hu, H. Luo, S. Wen, and Z. Liu, "Broadband photonic spin Hall meta-lens," ACS Nano **12**, 82–88 (2018).
32. X. F. Zang, B. S. Yao, Z. Li, Y. Zhu, J. Y. Xie, L. Chen, A. V. Balakin, A. P. Shkurinov, Y. M. Zhu, and S. L. Zhuang, "Geometric phase for multidimensional manipulation of photonics spin Hall effect and helicity-dependent imaging," Nanophotonics **9**, 1501–1508 (2020).
33. X. J. Ni, A. V. Kildishev, V. M. Shalaev, and M. Vladimir, "Metasurface holograms for visible light," Nat. Commun. **4**, 2807 (2013).

34. G. Zheng, H. Mühlenbernd, M. Kenney, G. Li, T. Zentgraf, and S. Zhang, "Metasurface holograms reaching 80% efficiency," Nat. Nanotechnol. **10**, 308–312 (2015).
35. D. Wen, D. F. Yue, G. Li, G. Zheng, K. Chan, S. Chen, M. Chen, K. F. Li, P. W. H. Wong, K. W. Cheah, E. Y. B. Pun, S. Zhang, and X. Chen, "Helicity multiplexed broadband metasurface holograms," Nat. Commun. **6**, 8241 (2015).
36. X. Li, L. W. Chen, Y. Li, X. H. Zhang, M. B. Pu, Z. Y. Zhao, X. L. Ma, Y. Q. Wang, M. H. Hong, and X. G. Luo, "Multicolor 3D meta-holography by broadband plasmonic modulation," Sci. Adv. **2**, e1601102 (2016).
37. L. Jin, Z. Dong, S. Mei, Y. Yu, Z. Wei, Z. Pan, S. Rezaei, X. Li, A. I. Kuznetsov, Y. S. Kivshar, J. K. W. Yang, and C. W. Qiu, "Noninterleaved metasurface for (2^6 – 1) spin- and wavelength-encoded holograms," Nano Lett. **18**, 8016–8024 (2018).
38. L. Jin, Y. W. Huang, Z. Jin, R. C. Devlin, Z. Dong, S. Mei, M. Jiang, W. T. Chen, Z. Wei, H. Liu, J. Teng, A. Danner, X. Li, S. Xiao, S. Zhang, C. Yu, J. K. W. Yang, F. Capasso, and C. W. Qiu, "Dielectric multi-momentum meta-transformer in the visible," Nat. Commun. **10**, 4789 (2019).
39. Q. Song, A. Baroni, R. Sawant, P. Ni, V. Brandli, S. Chenot, S. Vezian, B. Damilano, P. de Mierry, S. Khadir, P. Ferrand, and P. Genevet, "Ptychography retrieval of fully polarized holograms from geometric-phase metasurfaces," Nat. Commun. **11**, 2651 (2020).
40. G. X. Li, S. M. Chen, N. Pholchai, B. Reineke, P. W. H. Wong, E. Y. B. Pun, K. W. Cheah, T. Zentgraf, and S. Zhang, "Continuous control of the nonlinearity phase for harmonic generations," Nat. Mater. **14**, 607–612 (2015).
41. W. Ye, F. Zeuner, X. Li, B. Reineke, S. He, C. W. Qiu, J. Liu, Y. Wang, S. Zhang, and T. Zentgraf, "Spin and wavelength multiplexed nonlinear metasurface holography," Nat. Commun. **7**, 11930 (2016).
42. Z. Li, W. Liu, Z. Li, C. Tang, H. Cheng, J. Li, X. Chen, S. Chen, and J. Tian, "Tripling the capacity of optical vortices by nonlinear metasurface," Laser Photon. Rev. **12**, 1800164 (2018).
43. G. Hu, X. Hong, K. Wang, J. Wu, H.-X. Xu, W. Zhao, W. Liu, S. Zhang, F. Garcia-Vidal, B. Wang, P. Lu, and C. W. Qiu, "Coherent steering of nonlinear chiral valley photons with a synthetic Au–WS_2 metasurface," Nat. Photonics **13**, 467–472 (2019).
44. A. Arbabi, Y. Horie, M. Bagheri, and A. Faraon, "Dielectric metasurfaces for complete control of phase and polarization with subwavelength spatial resolution and high transmission," Nat. Nanotechnol. **10**, 937–943 (2015).
45. H. Cheng, Z. Liu, S. Chen, and J. Tian, "Emergent functionality and controllability in few-layer metasurfaces," Adv. Mater. **27**, 5410–5421 (2015).
46. E. Maguid, I. Yulevich, D. Veksler, V. Kleiner, M. L. Brongersma, and E. Hasman, "Photonic spin-controlled multifunctional shared-aperture antenna array," Science **352**, 1202–1206 (2015).
47. Y. Yuan, K. Zhang, B. Ratni, Q. Song, X. Ding, Q. Wu, S. N. Burokur, and P. Genevet, "Independent phase modulation for quadruplex polarization channels enabled by chirality-assisted geometric-phase metasurfaces," Nat. Commun. **11**, 4186 (2020).
48. K. Zhang, Y. Yuan, X. Ding, H. Li, B. Ratni, Q. Wu, J. Liu, S. N. Burokur, and J. Tan, "Polarization-engineered noninterleaved metasurface for integer and fractional orbital angular momentum multiplexing," Laser Photon. Rev. **15**, 2000351 (2020).
49. F. Yue, D. Wen, J. Xin, B. D. Gerardot, J. Li, and X. Chen, "Vector vortex beam generation with a single plasmonic metasurface," ACS Photon. **3**, 1558–1563 (2016).
50. Y. J. Bao, J. C. Ni, and C. W. Qiu, "A minimalist single-layer metasurface for arbitrary and full control of vector vortex beams," Adv. Mater. **32**, 1905659 (2020).
51. Y. Zhang, W. Liu, J. Gao, and X. Yang, "Generating focused 3D perfect vortex beams by plasmonic metasurfaces," Adv. Opt. Mater. **6**, 1701228 (2018).
52. J. Han, Y. Intaravanne, A. Ma, R. Wang, S. Li, Z. Li, S. Chen, J. Li, and X. Chen, "Optical metasurfaces for generation and superposition of optical ring vortex beams," Laser Photon. Rev. **14**, 2000146 (2020).
53. M. Liu, P. Huo, W. Zhu, C. Zhang, S. Zhang, M. Song, S. Zhang, Q. Zhou, L. Chen, H. J. Lezec, A. Agrawal, Y. Lu, and T. Xu, "Broadband generation of perfect Poincaré beams via dielectric spin-multiplexed metasurface," Nat. Commun. **12**:2230 (2021).
54. J. Xie, H. Guo, S. Zhuang, and J. Hu, "Polarization-controllable perfect vortex beam by a dielectric metasurface," Opt. Express **29**, 3081–3089 (2021).
55. F. Yue, D. Wen, C. Zhang, B. D. Gerardot, W. Wang, S. Zhang, and X. Chen, "Multichannel polarization-controllable superpositions of orbital angular momentum states," Adv. Mater. **29**, 1603838 (2017).
56. H. Zhao, B. Quan, X. Wang, C. Gu, J. Li, and Y. Zhang, "Demonstration of orbital angular momentum multiplexing and demultiplexing based on a metasurface in the terahertz band," ACS Photon. **5**, 1726–1732 (2017).
57. Y. Li, X. Li, L. Chen, M. Pu, J. Jin, M. Hong, and X. Luo, "Orbital angular momentum multiplexing and demultiplexing by a single metasurface," Adv. Opt. Mater. **5**, 1600502 (2015).
58. Y. Ou, M. Zhang, F. Zhang, J. Cai, and H. Yu, "All-dielectric metasurfaces for generation and detection of multi-channel vortex beams," Appl. Phys. Express **12**, 082004 (2019).
59. S. Zhang, P. Huo, W. Zhu, C. Zhang, P. Chen, M. Liu, L. Chen, H. J. Lezec, A. Agrawal, Y. Lu, and T. Xu, "Broadband detection of multiple spin and orbital angular momenta via dielectric metasurface," Laser Photon. Rev. **14**, 2000062 (2020).
60. S. Liu, C. Li, J. Liu, L. Zhu, Z. Xu, J. Zhou, Q. Yang, and J. Wang, "Multiple orbital angular momentum (OAM) modes (de)multiplexer based on single complex phase mask," in *European Conference on Optical Communication (ECOC)* (2014).
61. P. Huo, C. Zhang, W. Zhu, M. Liu, S. Zhang, S. Zhang, L. Chen, H. J. Lezec, A. Agrawal, Y. Lu, and T. Xu, "Photonic spin-multiplexing metasurface for switchable spiral phase contrast imaging," Nano Lett. **20**, 2791–2798 (2020).
62. J. Hu, D. Wang, D. Bhowmik, T. Liu, S. Deng, M. P. Knudson, X. Ao, and T. W. Odom, "Lattice-resonance metalenses for full reconfigurable imaging," ACS Nano **13**, 4613–4620 (2019).
63. S. Colburn, A. Zhan, and A. Majumdar, "Metasurface optics for full-color computational imaging," Sci. Adv. **4**, eaar2114 (2018).